

Homogeneously Mixing Different Metal–Organic Framework Structures in Single Nanocrystals through Forming Solid Solutions

Ming Xu,[#] Sha-Sha Meng,[#] Peiyu Cai,[#] Yu-Hao Gu, Tong-An Yan, Tian-Hao Yan, Qing-Hua Zhang, Lin Gu, Da-Huan Liu, Hong-Cai Zhou,^{*} and Zhi-Yuan Gu^{*}



Cite This: *ACS Cent. Sci.* 2022, 8, 184–191



Read Online

ACCESS |



Metrics & More

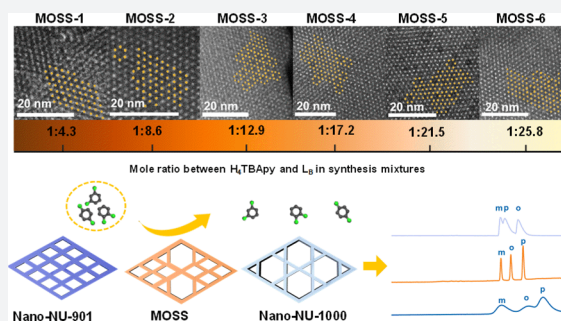


Article Recommendations



Supporting Information

ABSTRACT: Pore engineering plays a significant role in the applications of porous materials, especially in the area of separation and catalysis. Here, we demonstrated a metal–organic framework (MOF) solid solution (MOSS) strategy to homogeneously and controllably mix NU-1000 and NU-901 structures inside single MOF nanocrystals. The key for the homogeneous mixing and forming of MOSS was the bidentate modulator, which was designed to have a slightly longer distance between two carboxylate groups than the original tetratopic ligand. All of the MOSS nanocrystals showed a uniform pore size distribution with a well-tuned ratio of mesopores to micropores. Because of the appropriate pore ratio, MOSS nanocrystals can balance the thermodynamic interactions and kinetic diffusion of the substrates, thus showing exceedingly higher separation abilities and a unique elution sequence. Our work proposes a rational strategy to design mixed-porous MOFs with controlled pore ratios and provides a new direction to design homogeneously mixed MOFs with a high separation ability and unique separation selectivity.



INTRODUCTION

Engineering pores, including pore sizes, pore shapes, and pore environments of porous materials, has prompted numerous advances in a wide range of applications, especially in separation and catalysis.^{1–4} Matching the pore shape and size between target molecules and the porous materials has led to the discovery of many highly efficient catalysts and separation materials.^{5–7} Currently, the state-of-the-art strategy requires a rigorous control of pore shape and size in the narrow distribution for the ordered porous materials to accommodate the target molecule.^{8–11} Moreover, too small pores bring inaccessible sites and large diffusion barriers, while too large pores reduce the interactions between target substrates and the porous materials.^{12,13} The above mismatching leads to both an unbalanced thermodynamic interaction and kinetic diffusion, resulting in low separation and catalytic performances. An alternative strategy to improve the performance with the consideration of both diffusion and interaction is to utilize a material with well-tuned small and large pores.¹⁴ However, material synthesis and pore modulation are currently a challenge.

Highly ordered metal–organic frameworks (MOFs) epitomize devisable platforms to form functional materials with mixed pores. This is because of the diversity of inorganic metal clusters and organic ligands, the designable pore shape and size, and the coordination control through the use of different modulators.^{15–17} However, it is still exceedingly demanding to

optimize the ratio of different kinds of pores in a single MOF.^{18,19} Some approaches have been attempted to create mesopores in the original microporous MOFs. For example, applying micelles as templates or using thermally labile organic linkers as coligands are effective ways to synthesize mixed-porous MOFs.^{20–23} The obtained MOFs are usually with low crystallinity and random pore size distributions. Meanwhile, it is inevitable for undesired macropores to be introduced with these methods. Another effective way to obtain mixed-porous MOFs is to form MOF heterostructures in single crystals.^{17,24–27} However, the ratio of MOF structures in these MOFs is hard to control, and the distribution of different MOF phases is usually isolated and fixed.^{24,25,28–30}

To address these challenges, we demonstrated an MOF solid solution(s) (MOSS) strategy, which generated homogeneous MOF single nanocrystals through mixing two different micropore and mesopore MOF structures. Previously, the MOSS was recognized as MOFs with different mixed metals or ligands in the same MOF structures.^{31–35} Homogeneously mixing the micropores and mesopores in uniform nanocrystals

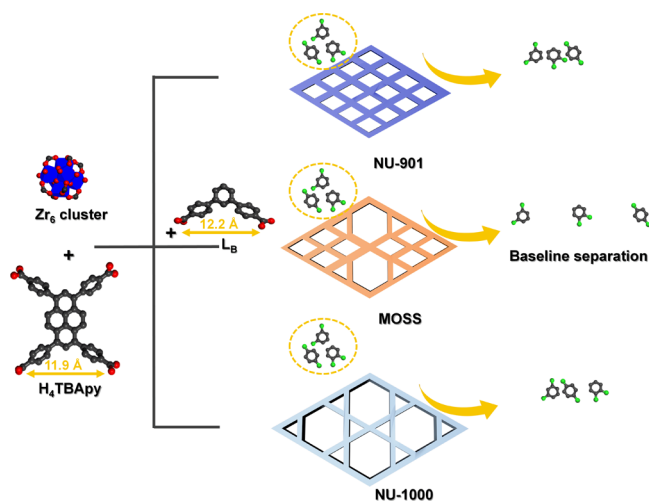
Received: November 2, 2021

Published: January 25, 2022



with the same metal and ligand is still challenging and has not been explored yet. The zirconium MOF NU-901 with scu topology and NU-1000 with csq topology were chosen as the model structures because these two MOFs share the same metal nodes and organic linker H_4TBAPy ($H_4TBAPy = 1,3,6,8$ -tetrakis(*p*-benzoic acid)pyrene) but exhibit different microporous and mesoporous structures, respectively (Scheme 1).^{36,37} Meanwhile, the topologies of tetracarboxylate MOFs (flu, scu, or csq) can be targeted by changing the size of tetratopic ligands.^{38,39}

Scheme 1. Schematic Diagram of Modulating the Separation Ability of Porous Materials via the MOSS Strategy through Engineering Pore Size and Shape in Single MOF Nanocrystals



In this work, to homogeneously mix the csq topology with the scu topology, the bidentate ligand L_B ($L_B = [1,1',3',1''$ -terphenyl]-4,4''-dicarboxylic acid) with a slightly longer distance between two carboxylate groups (12.2 Å) than H_4TBAPy (11.9 Å) (Scheme 1) was designed as the modulator. Then, MOSSs were obtained which mixed the csq topology and scu topology in the same material with a uniform pore size distribution without creating other phases or large macropores. Furthermore, the ratio of mesopores to micropores was well-tuned by modulating the ratio of bidentate to tetratopic ligands. The addition of L_B (molar ratio of H_4TBAPy to $L_B = 1:4.3, 1:8.6, \text{ and } 1:12.9$) results in MOSS-1, MOSS-2, and MOSS-3, respectively, and significantly enhances the volume ratio of mesopores to micropores from 0:1 of NU-901 to 0.2:1, 0.3:1, and 1:1, respectively.

Further applications of MOSS as the stationary phase for gas chromatography (GC) were explored and compared with nano-NU-901, nano-NU-1000, and NU-1000/NU-901/NU-1000 heterostructures. The MOSS showed greatly improved separation abilities over other materials. The MOSS also shows quite different elution sequences, indicating the potential of a different separation mechanism. Grand canonical Monte Carlo (GCMC) and molecular dynamic (MD) simulations as well as the diffusion coefficient measurement were utilized to understand the separation mechanism. The results of simulations and experiments proved that the MOSS balanced the thermodynamic interactions and kinetic diffusion to enhance their separation ability. This MOSS strategy using bidentate ligands provides a new direction to homogeneously

mix different MOF structures in single MOF nanocrystals with modulated pore size distributions and presents an opportunity to design high-performance MOF separators.

RESULTS AND DISCUSSION

Powder X-ray Diffraction (PXRD) Patterns. Here, a series of MOSSs with L_B as a modulator (molar ratio of H_4TBAPy to $L_B = 1:4.3, 1:8.6, 1:12.9, 1:17.2, 1:21.5, \text{ and } 1:25.8$) and nano-NU-901 without L_B as a modulator were synthesized (Figures S1–S12). To confirm the structures of the synthesized MOSS, PXRD patterns of all of the materials were collected and compared with the simulated PXRD patterns of NU-901 and NU-1000, respectively (Figure 1a).

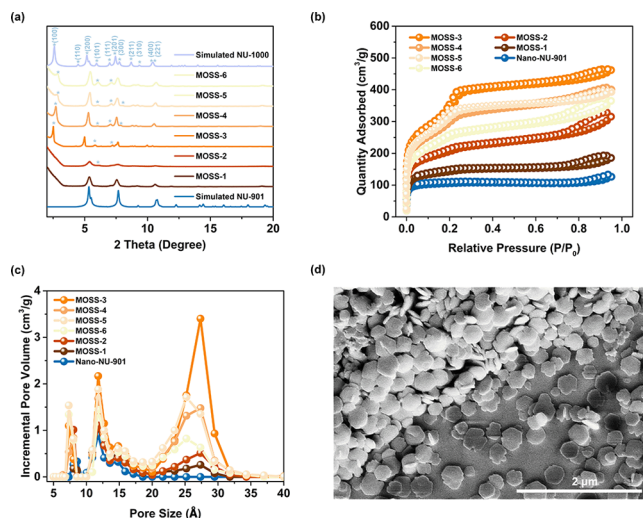
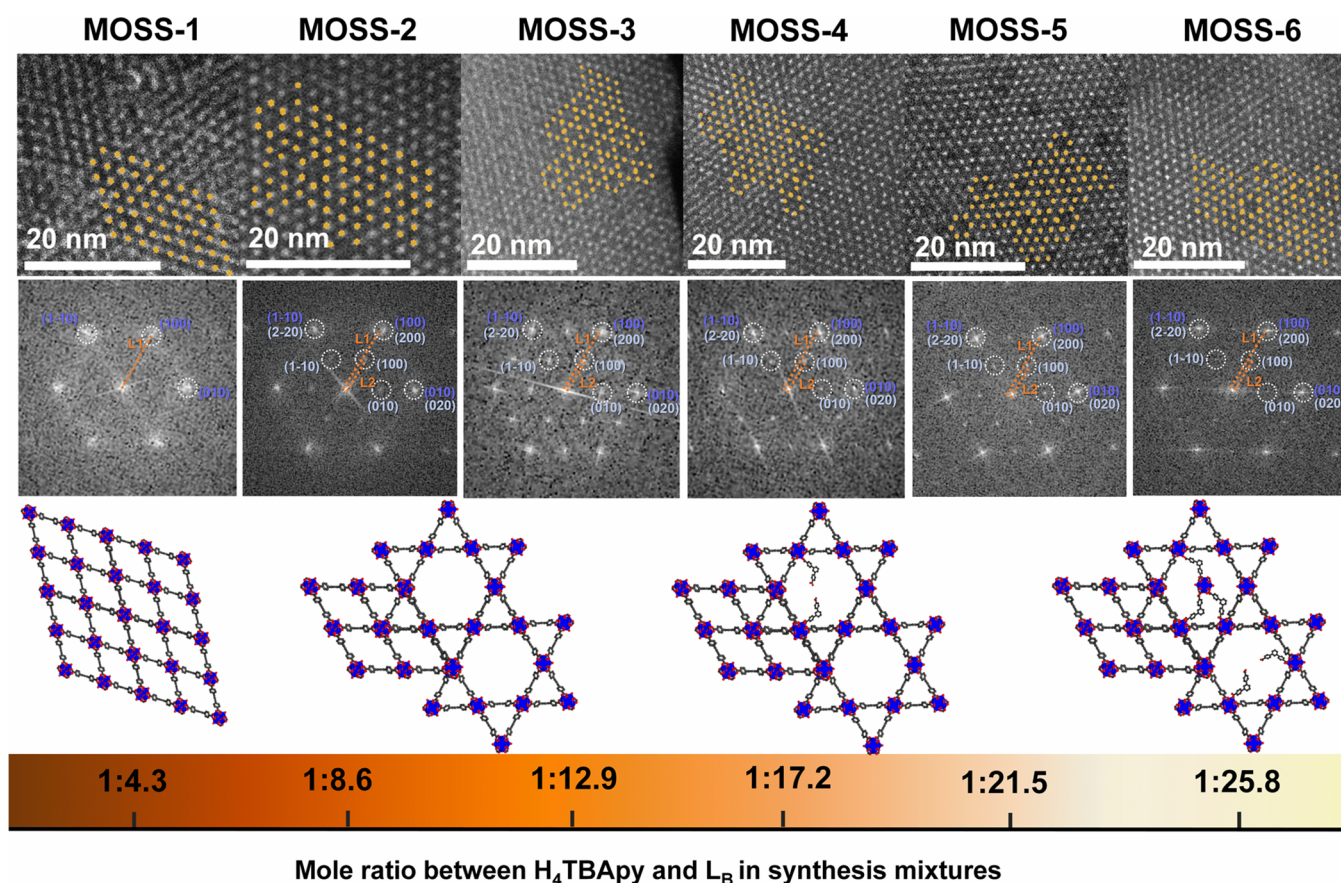


Figure 1. (a) PXRD patterns of MOSS-1, MOSS-2, MOSS-3, MOSS-4, MOSS-5, MOSS-6, simulated NU-901, and simulated NU-1000. (b) N_2 adsorption–desorption isotherms at 77 K and (c) pore size distribution (DFT method) of MOSS-1, MOSS-2, MOSS-3, MOSS-4, MOSS-5, MOSS-6, and nano-NU-901. (d) SEM images of MOSS-3.

The broadening of peaks results from the small particle sizes and thin thickness of the obtained materials.⁴⁰ Without the L_B modulator, nano-NU-901 shows the same PXRD pattern with the simulated pattern (Figure S1). After the addition of the L_B modulator, MOSS-1 and MOSS-2 still show PXRD patterns similar to that of the pure NU-901, which indicates the structure similarity of MOSS-1 and MOSS-2 compared to NU-901. When the ratio of L_B increases, MOSS-3, MOSS-4, MOSS-5, and MOSS-6 all exhibit diffraction peaks similar to those of NU-1000 at about $2.6^\circ, 6.0^\circ, 7.0^\circ, \text{ and } 7.8^\circ$, which represent (100), (101), (111), and (300) planes of the structure, respectively. This phenomenon proves the existence of the NU-1000 structure in the four MOSS structures above. It is worth noting that the diffraction peaks of MOSS-3 shift to a lower 2θ angle, and the diffraction peaks of MOSS-4, MOSS-5, and MOSS-6 shift to a higher 2θ angle compared with NU-1000.^{19,41–43} These phenomena demonstrate that the cell parameters of MOSS are different from both NU-901 and NU-1000. Considering that the diffraction peaks do not shift when different MOFs are physically mixed or coexist in heterostructures, it suggests that NU-901 and NU-1000 structures are mixed homogeneously in MOSS.^{17,44–47} For a further understanding of how the structures were mixed in MOSS, the cell parameters of MOSS can be calculated from the PXRD patterns after the Pawley refinement by Material Studio 7.0



Mole ratio between H_4TBAPy and L_B in synthesis mixtures

Figure 2. HAADF images and the corresponding FFT patterns of MOSS-1, MOSS-2, MOSS-3, MOSS-4, MOSS-5, and MOSS-6. For clarity, all FFT patterns are rotated in the same direction. The diffraction spots labeled with light blue and dark blue are attributed to the plane of NU-1000 and NU-901, respectively. The schematic structure of the synthesized materials.

software (Table S1 and Figure S12). It was found that the a -axis of MOSS is different from those of both simulated NU-901 and NU-1000. With the least L_B modulator, the cell parameter of MOSS-1 is similar to that of NU-901. With an increased L_B modulator amount in MOSS-3 and MOSS-4, the a -axis length sequentially increases to the a -axis length of simulated NU-1000. The phenomena illustrate that, with less L_B in the synthetic mixture, the $ZrCl_4$ and H_4TBAPy ligands will form the NU-901-like structure. Meanwhile, the addition of L_B will compete with the H_4TBAPy ligands to coordinate with Zr_6 clusters, introducing the NU-1000 structure with a csq topology into the material. When the ratio of L_B further increases, the a -axis length of MOSS-5 and MOSS-6 sequentially decreases compared with NU-1000. Too much L_B may coordinate on the exposed Zr-sites around the mesopores of MOSS, forming the NU-901-like structure, thus leading to the shortened a -axis length. A similar phenomenon has been observed when synthesizing multi-component MOFs through the subsequent incorporation of organic linkers and metal clusters into the cavity of a mesoporous MOF.⁴⁸

To further validate the role of the L_B modulator, a density functional theory (DFT) simulation was performed to examine the relative stabilities of the H_4TBAPy ligand and L_B ligand in NU-901 and NU-1000 structures with Material Studio 7.0 software (see the Supporting Information for details). The energy of the H_4TBAPy ligand in NU-901 is 19.4 kJ/mol lower than that in NU-1000. Contrarily, the energy of the L_B ligand in NU-1000 is 5.06 kJ/mol lower than that in NU-901. Thus,

the L_B ligand prefers to form NU-1000 with a csq topology. The conclusion is in accordance with the reported results that it is easier for the tetracarboxylate ligands, which have a slightly longer distance between two carboxylate groups, to form a csq topology than H_4TBAPy .³⁹ A control experiment was done with a slightly shorter ligand, 4,4'-sulfonyldibenzoic acid as the modulator, replacing the L_B ligand in the synthetic procedure. The PXRD patterns show that there is no csq topology mixed in these materials (Figure S11). The phenomenon again proves the importance of the ligand size in modulating the topology of zirconium MOFs.

It should be noted that the synthesis of MOSS requires both the tetraprotic linker H_4TBAPy and the bidentate modulator L_B . Only L_B and $ZrCl_4$ without H_4TBAPy ligands cannot form MOSS structures under similar synthetic conditions. The NMR results of the digested MOSS were quantitatively analyzed to evaluate the ratio of H_4TBAPy and L_B in these materials (Figure S13–16 and Table S2). With more L_B added into the synthesis reaction, the ratio of L_B ligands to H_4TBAPy ligands increases, and the ratio of acetate to H_4TBAPy ligands reduces. This phenomenon proves that the L_B ligands replace the acetate and competitively coordinate with the exposed Zr-sites. Besides, the L_B ligands will cover the surface of MOSS, preventing the continual growth.

TEM, SEM, and High-Angle Annular Dark-Field (HAADF) Images. To further prove that the synthesized MOSSs are not simple particle mixtures or MOF heterostructures of NU-1000 and NU-901, TEM and SEM images of all MOSSs were collected (Figure 1d and Figures S2–S7).

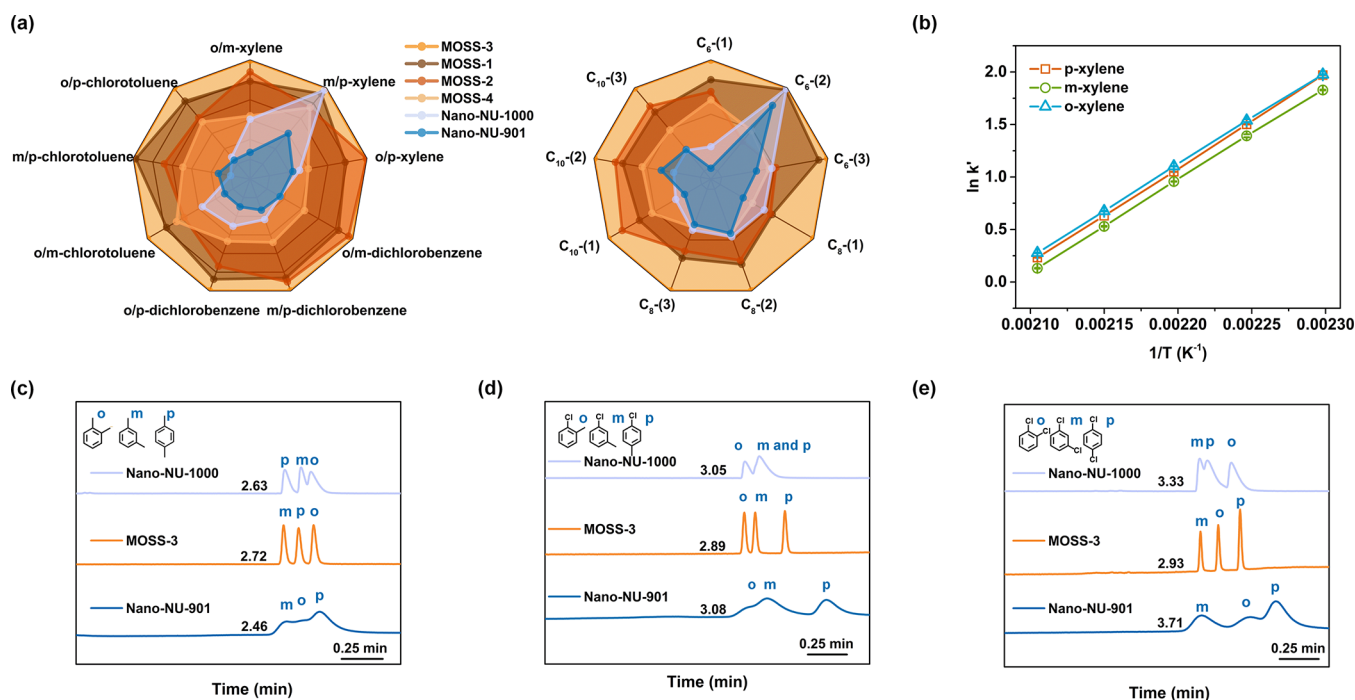


Figure 3. Separation performance of MOSS. (a) Separation resolution for disubstituted benzene isomers (left) and alkane isomers (right) on the MOSS-1, MOSS-2, MOSS-3, MOSS-4, nano-NU-901, and nano-NU-1000 coated GC columns. C₆-(1), C₆-(2), and C₆-(3) represent 2-methylpentane/3-methylpentane, 3-methylpentane/*n*-hexane, and 2-methylpentane/*n*-hexane, respectively. C₈-(1), C₈-(2), and C₈-(3) represent 2,4-dimethylhexane/3-methylheptane, 3-methylheptane/*n*-octane, and 2,4-dimethylhexane/*n*-octane, respectively. C₁₀-(1), C₁₀-(2), and C₁₀-(3) represent 4,4-dimethyloctane/3,3-dimethyloctane, 3,3-dimethyloctane/*n*-decane, and 4,4-dimethyloctane/*n*-decane, respectively. The scale was normalized to MOSS-3. (b) van't Hoff plots for xylene isomers on the MOSS-3 coated column. Gas chromatograms of (c) xylene, (d) chlorotoluene, and (e) dichlorobenzene isomers using MOSS-3, nano-NU-901, and nano-NU-1000 coated GC columns.

There is only one morphology in the obtained MOSS particles which look like nanosheets confirmed by both TEM and SEM images. The darker spindlelike particle in TEM images represents the standing MOSS nanosheets, which can also be supported by the SEM images (Figures S2–S7). This morphology is unique and largely different from the existing morphologies of nano-NU-901 (interpenetrated nanosheets, Figure S1), nano-NU-1000 (spindles, Figure S1), and NU-1000/NU-901/NU-1000 heterostructures (Figure S8). This is because the addition of L_B covers the surface of the materials and reduces their surface energy, leading to the nanosheet morphology with a small particle size and thin thickness. The hypothesis can be supported by the phenomenon that more L_B results in thinner MOSS, such as MOSS-6 (Figure S7).

To further investigate the structure of MOSS, HAADF images of all MOSSs were obtained (Figure 2). Similar to the TEM and SEM imaging results, HAADF images also support that only one phase with the nanosheet morphology exhibits for each MOSS structure. The white dots represent the Zr₆ clusters in the corresponding materials.^{49,50} The brighter samples result from the standing of the nanosheets (Figures S2–S7). In MOSS-1, six Zr₆ clusters form a hexagon with an additional Zr₆ cluster in the center of this hexagon, which is topologically the same as the rhombic crystal structure of NU-901. Besides, the corresponding fast Fourier transform (FFT) pattern of MOSS-1 shows a single set of hexagonal-shaped diffraction spots with the same brightness. From the distance between one spot and the hexagonal center (L1 ≈ 0.58 nm⁻¹), the *d* value in MOSS-1 can be calculated as 1.72 nm, which equals the *d* value of the (100) plane in simulated NU-901 (*d* = 1.65 nm). However, in MOSS-2, another structure appears:

six Zr₆ clusters form a hollow hexagon with no extra Zr₆ cluster in the center, which is the same as the NU-1000 structure. The phenomenon proves the existence of several NU-1000 structures in the structure of MOSS-2. As far as we know, this is the first time that the atomic-level homogeneous distributions of two MOF structures featuring the same metals and ligands (Zr₆ clusters and TBAPy) have been directly imaged in a single MOF through the HAADF technique. It mainly benefits from the thin thickness of MOSS. Meanwhile, different from the FFT pattern of MOSS-1, the FFT pattern of MOSS-2 has two sets of hexagonal-shaped diffraction spots with different brightnesses. The *d* value calculated from the L1 (L1 set) measured in the brighter set is consistent with the *d* value of the (100) plane in simulated NU-901 and the (200) plane in simulated NU-1000 (*d* = 1.70 nm), while the *d* value calculated from L2 (0.33 nm⁻¹, L2 set) in the other set is 3.03 nm, which is only in agreement with the *d* value of the (100) plane in the simulated NU-1000 (*d* = 3.42 nm). These phenomena prove that MOSS-2 mixed NU-901 and NU-1000 structures homogeneously in a single MOF nanocrystal, although the majority structure remains NU-901. From MOSS-2 to MOSS-3, more hollow hexagons appear which indicates that the ratio of NU-1000 structure to NU-901 structure increases. The *d* value calculated from L1 and L2 in MOSS-3 is 1.64 and 3.13 nm, respectively. The diffraction spots of the L1 set show almost the same brightness as the L2 set, indicating the higher ratio of NU-1000 structure to NU-901 structure in MOSS-3 than in other MOSSs. Although MOSS-4, MOSS-5, and MOSS-6 form a similar solid solution of NU-901 and NU-1000, the appearance of hollow hexagons reduces compared with MOSS-3. This phenomenon is

consistent with their PXRD data and *a*-axis lengths. It is possibly caused by the excess of the L_B modulators which bind to both the exposed Zr-sites around the mesopores and the additional Zr_6 clusters in the synthesis mixtures, forming the NU-901-like structure. Besides, the FFT patterns measured in different regions of single MOSS-4, MOSS-5, and MOSS-6 particles are identical, proving that NU-901 and NU-1000 structures in MOSS are mingled homogeneously in single MOF nanocrystals to form a solid solution (Figure S9). From these results, MOSSs which mingle the structures of NU-901 and NU-1000 are successfully synthesized using the L_B as a modulator. The ratio between the two structures can be well-tuned by carefully controlling the amount of the L_B modulator.

Pore Size Distribution. To further characterize the porosities of MOSSs, their N_2 adsorption isotherms were also recorded and compared with nano-NU-901 and nano-NU-1000. As shown in Figure 1b,c, the nano-NU-901 has the lowest N_2 adsorption, the lowest Brunauer–Emmett–Teller (BET) surface area ($381 \text{ m}^2/\text{g}$), as well as no mesopores. This phenomenon proves the bulk phase purity of nano-NU-901. Meanwhile, nano-NU-1000 has the highest N_2 adsorption, the highest BET surface area ($1826 \text{ m}^2/\text{g}$), and the highest mesopore to micropore ratio (1.75:1) (Figure S10). From nano-NU-901 to MOSS-1, MOSS-2, and MOSS-3, the N_2 adsorption and the BET surface area increase accordingly (Table S3). This obvious increase is contributed by the increment of the mesopores in these MOSS. Table S3 shows that the ratio of mesopores to micropores has improved from 0:1 to 1:1, which confirms again that the addition of L_B introduces mesopores into the material, and the ratio of mesopores to micropores is well-tuned. Notably, the N_2 adsorption isotherms also show that the MOSS-4, MOSS-5, and MOSS-6 have lower N_2 adsorption, as well as a lower BET surface area than MOSS-3. This phenomenon also proves that the coordinated L_B itself and further dangled Zr_6 clusters reduce the pore size of the mesopores.

Separation Performance of MOSS. The successful modulation of micropores and mesopores in MOSS encourages us to investigate the separation abilities of these materials. To make a fair comparison and avoid the diffusion barrier in MOF large crystals, nanosized MOF counterparts were used for control experiments. MOSS from MOSS-1–MOSS-4 as well as nano-NU-901 and nano-NU-1000 were coated on the inner wall of capillary columns and utilized as stationary phases for isomer separations (Figure S17). It should be noted here that the coating procedure will not influence the structure and the morphology of MOFs which have been proved by the previous works and the SEM images of the MOSS-2 and MOSS-3 coated in the capillary columns (Figures S18 and S19). The loading quantity of all materials is calculated to slightly vary between 1.0 and 1.2 mg.^{14,51} The SEM images show that all of the materials are coated uniformly (Figure S17). These columns were aged at $250 \text{ }^\circ\text{C}$ for 180 min to remove the guest molecules according to the thermogravimetric analysis of MOSS (Figure S20).

Six groups of disubstituted benzene isomers and alkane isomers were utilized to test the separation ability of the materials obtained. The nano-NU-901 and nano-NU-1000 exhibit poor performance due to their intrinsic pore properties (Figure 3). The nano-NU-901 with only micropores results in a good selectivity (α) of isomers, indicating the strong thermodynamic interactions (Figure 3a, Figures S21–S24 and Table S4). However, the severe peak broadening on the

nano-NU-901 caused by large kinetic diffusion barriers leads to the overall low separation resolution (R_s , Table S5) and column efficiency [the theoretical plate number (N) = 120 plates/m]. While the nano-NU-1000 with a large fixed amount of mesopores provides a slightly higher R_s than nano-NU-901 with reduced peak broadening, its low interactions with analytes still result in low separation performance. The low separation abilities of both nano-NU-901 and nano-NU-1000 prove that the nano-MOFs with unbalanced kinetic diffusion and thermodynamic interactions are inappropriate to be applied as a high-performance GC stationary phase. As a comparison, the MOF-heterostructures (NU-1000/NU-901/NU-1000 heterostructure) were also synthesized and tested as the stationary phase for separating the same mixtures as another control experiment. The material exhibits no separation ability at all to separate xylene isomers, indicating that the formation of MOF heterostructures still cannot balance the kinetic diffusion and thermodynamic interactions (Figure S25).

However, different from the nano-NU-901, nano-NU-1000, and NU-1000/NU-901/NU-1000 heterostructure, the MOSSs homogeneously mingle micropores and mesopores in single particles, which can balance the kinetic diffusion and thermodynamic interactions. Thus, MOSS-1, MOSS-2, MOSS-3, and MOSS-4 exhibit significantly higher separation abilities than the former three materials (Figure 3a,c–e and Figures S21–S29). Among the four MOSS structures, MOSS-3 with a 1:1 mesopore-to-micropore ratio provides the highest separation performance with minimal peak broadening and tailing. The optimized ratio of mesopores and micropores balances the kinetic diffusion barrier and the thermodynamic interactions to achieve high column efficiency ($N = 3657$ plates/m) and high separation resolution (Table S5). Furthermore, the MOSS-3 coated column exhibits a better separation ability than commercial columns. For example, the resolution for *m*-xylene and *p*-xylene ($R_s = 1.17$) in MOSS-3 is much better than those in HP-5MS ($R_s = 0$) and VF-WAXMS ($R_s = 0.47$) (Table S5).⁵² Besides, the MOSS-3 synthesized after about eight months still shows a good ability to separate dichlorobenzene isomers, and the separation ability of the material exhibits no difference after heating up to $250 \text{ }^\circ\text{C}$ and cooling to $100 \text{ }^\circ\text{C}$ 50 times (Figure S30). These phenomena prove the good stability of the MOSS-3 column. Notably, all MOSS coated columns exhibit outstanding separation abilities to disubstituted benzene isomers and alkanes isomers, which indicates the high commercial value of these columns (Figure 3a).

It is also worthwhile to note that MOSS coated columns (e.g., MOSS-3) show a quite different selectivity toward *p*-xylene compared with nano-NU-901 and nano-NU-1000 coated columns (Figure 3c). In the nano-NU-1000 coated column, *p*-xylene exhibits the shortest elution time compared with *o*-xylene and *m*-xylene, while in the nano-NU-901 coated column, *p*-xylene exhibits the longest elution time compared with *o*-xylene and *m*-xylene. Different from both nano-NU-1000 and nano-NU-901 coated columns, *p*-xylene exhibits an intermediate elution time in the MOSS-3 coated column compared with *o*-xylene and *m*-xylene. To explain this unusual phenomenon, adsorption enthalpy (ΔH) and the diffusion constant (D_s) of all xylene isomers were measured and calculated via the van't Hoff equation and Golay equation, respectively (see the Supporting Information for details). The *p*-xylene in nano-NU-1000 shows the lowest ΔH and highest

D_s among the three isomers, indicating the weakest interaction and lowest diffusion barrier (Tables S8 and S11 and Figures S31 and S32). Thus, *p*-xylene elutes from the nano-NU-1000 first in comparison with other isomers. When it comes to nano-NU-901, *p*-xylene shows the largest ΔH among the three isomers (Tables S6–S8), because *p*-xylene with the smallest minimum cross diameter ($d_{p\text{-xylene}} = 6.63 \text{ \AA}$, $d_{o\text{-xylene}} = 7.25 \text{ \AA}$, $d_{m\text{-xylene}} = 7.27 \text{ \AA}$) enters the micropores with the weakest resistance, leading to the strongest thermodynamic interaction. Thus, *p*-xylene exhibits the longest elution time on the nano-NU-901 coated column. Different from the two nano-MOFs, MOSS-3 mingles the structures of NU-901 and NU-1000, balancing the thermodynamic interactions and the kinetic diffusion. The *p*-xylene shows the highest ΔH among the three isomers which proves the highest thermodynamic adsorption of *p*-xylene on the MOSS-3 (Tables S6–S8). Meanwhile, the *p*-xylene shows the highest D_s among all three isomers which exhibit the highest diffusion rate (Tables S9–S11). The highest ΔH drives *p*-xylene to elute last, while the highest D_s promotes *p*-xylene to elute first from the column. Thus, the opposite driving forces encourage *p*-xylene to exhibit the intermediate elution time on the MOSS-3 coated column. Notably, it is inappropriate to compare the value of ΔH and D_s of the same isomer on different columns because of the different column parameters and detection temperatures.

To further support the experimental explanation, the adsorption and diffusion behavior of xylene isomers was investigated via grand canonical Monte Carlo (GCMC) and molecular dynamics (MD) simulation. Compared with the other two isomers, *p*-xylene shows the largest isotropic heat of adsorption (Q_{st}) on the NU-901 and MOSS-3 coated columns (Table S12). Meanwhile, *p*-xylene shows the highest self-diffusion coefficient on the NU-1000 and MOSS-3 coated columns (Figure S33 and Table S13). The simulation results are in good accordance with the experimental data, illustrating that the MOSS strategy is an effective method to balance kinetic diffusion and thermodynamic interactions.

CONCLUSION

In summary, we demonstrated a MOSS strategy to introduce mesopores into microporous MOFs through mixing NU-901 and NU-1000 structures homogeneously in single MOF nanocrystals. The ratio of mesopores to micropores in MOSS could be well-tuned by controlling the amount of the bidentate ligands which are exactly half the size of the original tetradentate ligands. MOSS showed a uniform pore size distribution without undesirable macropores. This MOSS strategy provides a new method to synthesize MOFs with a precisely controlled micropore-to-mesopore ratio. All MOSSs showed much improved separation abilities as compared to nano-NU-901 and nano-NU-1000 due to the balance between the kinetic diffusion and thermodynamic interactions. Furthermore, MOSS showed a unique elution sequence of xylene isomers compared with nano-NU-901 and nano-NU-1000. This discovery unveils the excellent separation abilities of MOSS and can guide the design of next-generation high-performance stationary phases.

ASSOCIATED CONTENT

Supporting Information

The Supporting Information is available free of charge at <https://pubs.acs.org/doi/10.1021/acscentsci.1c01344>.

Experimental details, chemicals and instrumentation, synthesis details, characterizations, thermogravimetric analysis, HNMR, BET surface area, methods for preparing GC columns, GC separation, thermodynamic parameters, and computational simulation (PDF)

AUTHOR INFORMATION

Corresponding Authors

Hong-Cai Zhou – Department of Chemistry, Texas A&M University, College Station, Texas 77843-3255, United States; Department of Materials Science and Engineering, Texas A&M University, College Station, Texas 77842, United States; orcid.org/0000-0002-9029-3788; Email: zhou@chem.tamu.edu

Zhi-Yuan Gu – Jiangsu Key Laboratory of Biofunctional Materials, Jiangsu Collaborative Innovation Center of Biomedical Functional Materials, Jiangsu Key Laboratory of New Power Batteries, College of Chemistry and Materials Science, Nanjing Normal University, Nanjing 210023, China; orcid.org/0000-0002-6245-4759; Email: guzhiyuan@njnu.edu.cn

Authors

Ming Xu – Jiangsu Key Laboratory of Biofunctional Materials, Jiangsu Collaborative Innovation Center of Biomedical Functional Materials, Jiangsu Key Laboratory of New Power Batteries, College of Chemistry and Materials Science, Nanjing Normal University, Nanjing 210023, China

Sha-Sha Meng – Jiangsu Key Laboratory of Biofunctional Materials, Jiangsu Collaborative Innovation Center of Biomedical Functional Materials, Jiangsu Key Laboratory of New Power Batteries, College of Chemistry and Materials Science, Nanjing Normal University, Nanjing 210023, China

Peiyu Cai – Department of Chemistry, Texas A&M University, College Station, Texas 77843-3255, United States

Yu-Hao Gu – Jiangsu Key Laboratory of Biofunctional Materials, Jiangsu Collaborative Innovation Center of Biomedical Functional Materials, Jiangsu Key Laboratory of New Power Batteries, College of Chemistry and Materials Science, Nanjing Normal University, Nanjing 210023, China

Tong-An Yan – State Key Laboratory of Organic–Inorganic Composites, Beijing Advanced Innovation Center for Soft Matter Science and Engineering, Beijing University of Chemical Technology, Beijing 100029, China

Tian-Hao Yan – Department of Chemistry, Texas A&M University, College Station, Texas 77843-3255, United States; orcid.org/0000-0002-8900-3720

Qing-Hua Zhang – Institute of Physics, Chinese Academy of Sciences, Beijing 100190, China

Lin Gu – Institute of Physics, Chinese Academy of Sciences, Beijing 100190, China; orcid.org/0000-0002-7504-031X

Da-Huan Liu – State Key Laboratory of Organic–Inorganic Composites, Beijing Advanced Innovation Center for Soft Matter Science and Engineering, Beijing University of Chemical Technology, Beijing 100029, China; orcid.org/0000-0003-1005-3168

Complete contact information is available at: <https://pubs.acs.org/doi/10.1021/acscentsci.1c01344>

Author Contributions

#M.X., S.-S.M., and P.C. contributed equally.

Notes

The authors declare no competing financial interest.

ACKNOWLEDGMENTS

This work is supported by the National Natural Science Foundation of China (21922407 and 22174067), the Natural Science Foundation of Jiangsu Province of China (BK20190086), and the Priority Academic Program Development of Jiangsu Higher Education Institutions. Hong-Cai Zhou acknowledges financial support from the Robert A. Welch Foundation through a Welch Endowed Chair (A-0030). We thank Shuai Yuan at Nanjing University for the helpful discussion and suggestion.

REFERENCES

- (1) Meng, S.-S.; Xu, M.; Han, T.; Gu, Y.-H.; Gu, Z.-Y. Regulating Metal-Organic Frameworks as Stationary Phases and Absorbents for Analytical Separations. *Anal. Methods* **2021**, *13*, 1318–1331.
- (2) Zou, X.; Zhu, G. Microporous Organic Materials for Membrane-Based Gas Separation. *Adv. Mater.* **2018**, *30*, 1700750.
- (3) Wang, X.; Chi, C.; Zhang, K.; Qian, Y.; Gupta, K. M.; Kang, Z.; Jiang, J.; Zhao, D. Reversed Thermo-Switchable Molecular Sieving Membranes Composed of Two-Dimensional Metal-Organic Nanosheets for Gas Separation. *Nat. Commun.* **2017**, *8*, 14460.
- (4) Zhang, W.; Zheng, B.; Shi, W.; Chen, X.; Xu, Z.; Li, S.; Chi, Y. R.; Yang, Y.; Lu, J.; Huang, W.; et al. Site-Selective Catalysis of a Multifunctional Linear Molecule: The Steric Hindrance of Metal-Organic Framework Channels. *Adv. Mater.* **2018**, *30*, 1800643.
- (5) Chang, N.; Gu, Z.-Y.; Yan, X.-P. Zeolitic Imidazolate Framework-8 Nanocrystal Coated Capillary for Molecular Sieving of Branched Alkanes from Linear Alkanes Along with High-Resolution Chromatographic Separation of Linear Alkanes. *J. Am. Chem. Soc.* **2010**, *132*, 13645–13647.
- (6) Meng, S.-S.; Tao, Z.-R.; Tang, W.-Q.; Han, T.; Du, Y.; Gu, Z.-Y. Ultramicroporous Metal-Organic Frameworks for Capillary Gas Chromatographic Separation. *J. Chromatogr. A* **2020**, *1632*, 461604.
- (7) Wen, H.-M.; Liao, C.; Li, L.; Alsalmeh, A.; Allothman, Z.; Krishna, R.; Wu, H.; Zhou, W.; Hu, J.; Chen, B. A Metal-Organic Framework with Suitable Pore Size and Dual Functionalities for Highly Efficient Post-Combustion CO₂ Capture. *J. Mater. Chem. C* **2019**, *7*, 3128–3134.
- (8) Zhang, L.; Liu, X.; Dou, Y.; Zhang, B.; Yang, H.; Dou, S.; Liu, H.; Huang, Y.; Hu, X. Mass Production and Pore Size Control of Holey Carbon Microcages. *Angew. Chem., Int. Ed.* **2017**, *56*, 13790–13794.
- (9) Du, J.; Liu, L.; Hu, Z.; Yu, Y.; Qin, Y.; Chen, A. Order Mesoporous Carbon Spheres with Precise Tunable Large Pore Size by Encapsulated Self-Activation Strategy. *Adv. Funct. Mater.* **2018**, *28*, 1802332.
- (10) Ye, Y.; Ma, Z.; Lin, R.-B.; Krishna, R.; Zhou, W.; Lin, Q.; Zhang, Z.; Xiang, S.; Chen, B. Pore Space Partition within a Metal-Organic Framework for Highly Efficient C₂H₂/CO₂ Separation. *J. Am. Chem. Soc.* **2019**, *141*, 4130–4136.
- (11) He, T.; Huang, Z.; Yuan, S.; Lv, X.-L.; Kong, X.-J.; Zou, X.; Zhou, H.-C.; Li, J.-R. Kinetically Controlled Reticular Assembly of a Chemically Stable Mesoporous Ni(II)-Pyrazolate Metal-Organic Framework. *J. Am. Chem. Soc.* **2020**, *142*, 13491–13499.
- (12) Tao, Z.-R.; Wu, J.-X.; Zhao, Y.-J.; Xu, M.; Tang, W.-Q.; Zhang, Q.-H.; Gu, L.; Liu, D.-H.; Gu, Z.-Y. Untwisted Restacking of Two-Dimensional Metal-Organic Framework Nanosheets for Highly Selective Isomer Separations. *Nat. Commun.* **2019**, *10*, 2911.
- (13) Li, X.; Wang, J.; Bai, N.; Zhang, X.; Han, X.; da Silva, I.; Morris, C. G.; Xu, S.; Wilary, D. M.; Sun, Y.; et al. Refinement of Pore Size at Sub-Angstrom Precision in Robust Metal-Organic Frameworks for Separation of Xylenes. *Nat. Commun.* **2020**, *11*, 4280.
- (14) Gu, Z.-Y.; Yan, X.-P. Metal-Organic Framework MIL-101 for High-Resolution Gas-Chromatographic Separation of Xylene Isomers and Ethylbenzene. *Angew. Chem., Int. Ed.* **2010**, *49*, 1477–1480.
- (15) Xuan, W.; Zhu, C.; Liu, Y.; Cui, Y. Mesoporous Metal-Organic Framework Materials. *Chem. Soc. Rev.* **2012**, *41*, 1677–1695.
- (16) Lin, R.-B.; Li, L.; Zhou, H.-L.; Wu, H.; He, C.; Li, S.; Krishna, R.; Li, J.; Zhou, W.; Chen, B. Molecular Sieving of Ethylene from Ethane Using a Rigid Metal-Organic Framework. *Nat. Mater.* **2018**, *17*, 1128–1133.
- (17) Zhao, M.; Chen, J.; Chen, B.; Zhang, X.; Shi, Z.; Liu, Z.; Ma, Q.; Peng, Y.; Tan, C.; Wu, X.-J.; et al. Selective Epitaxial Growth of Oriented Hierarchical Metal-Organic Framework Heterostructures. *J. Am. Chem. Soc.* **2020**, *142*, 8953–8961.
- (18) Feng, L.; Day, G. S.; Wang, K.-Y.; Yuan, S.; Zhou, H.-C. Strategies for Pore Engineering in Zirconium Metal-Organic Frameworks. *Chem.* **2020**, *6*, 2902–2923.
- (19) Yuan, S.; Huang, L.; Huang, Z.; Sun, D.; Qin, J.-S.; Feng, L.; Li, J.; Zou, X.; Cagin, T.; Zhou, H.-C. Continuous Variation of Lattice Dimensions and Pore Sizes in Metal-Organic Frameworks. *J. Am. Chem. Soc.* **2020**, *142*, 4732–4738.
- (20) Feng, L.; Yuan, S.; Zhang, L.-L.; Tan, K.; Li, J.-L.; Kirchon, A.; Liu, L.-M.; Zhang, P.; Han, Y.; Chabal, Y. J.; et al. Creating Hierarchical Pores by Controlled Linker Thermolysis in Multivariate Metal-Organic Frameworks. *J. Am. Chem. Soc.* **2018**, *140*, 2363–2372.
- (21) Feng, L.; Lo, S.-H.; Tan, K.; Li, B.-H.; Yuan, S.; Lin, Y.-F.; Lin, C.-H.; Wang, S.-L.; Lu, K.-L.; Zhou, H.-C. An Encapsulation-Rearrangement Strategy to Integrate Superhydrophobicity into Mesoporous Metal-Organic Frameworks. *Matter* **2020**, *2*, 988–999.
- (22) Lo, S.-H.; Feng, L.; Tan, K.; Huang, Z.; Yuan, S.; Wang, K.-Y.; Li, B.-H.; Liu, W.-L.; Day, G. S.; Tao, S.; et al. Rapid Desolvation-Triggered Domino Lattice Rearrangement in a Metal-Organic Framework. *Nat. Chem.* **2020**, *12*, 90–97.
- (23) Liu, B.; Li, Y.; Oh, S. C.; Fang, Y.; Xi, H. Fabrication of a Hierarchically Structured HKUST-1 by a Mixed-Ligand Approach. *RSC Adv.* **2016**, *6*, 61006–61012.
- (24) Islamoglu, T.; Otake, K.-i.; Li, P.; Buru, C. T.; Peters, A. W.; Akpinar, I.; Garibay, S. J.; Farha, O. K. Revisiting the Structural Homogeneity of NU-1000, a Zr-Based Metal-Organic Framework. *CrystEngComm* **2018**, *20*, 5913–5918.
- (25) Garibay, S. J.; Jordanov, I.; Islamoglu, T.; DeCoste, J. B.; Farha, O. K. Synthesis and Functionalization of Phase-Pure NU-901 for Enhanced CO₂ Adsorption: The Influence of a Zirconium Salt and Modulator on the Topology and Phase Purity. *CrystEngComm* **2018**, *20*, 7066–7070.
- (26) Yu, J.; Park, J.; Van Wyk, A.; Rumbles, G.; Deria, P. Excited-State Electronic Properties in Zr-Based Metal-Organic Frameworks as a Function of a Topological Network. *J. Am. Chem. Soc.* **2018**, *140*, 10488–10496.
- (27) Webber, T. E.; Liu, W.-G.; Desai, S. P.; Lu, C. C.; Truhlar, D. G.; Penn, R. L. Role of a Modulator in the Synthesis of Phase-Pure NU-1000. *ACS Appl. Mater. Interfaces* **2017**, *9*, 39342–39346.
- (28) Noh, H.; Kung, C.-W.; Islamoglu, T.; Peters, A. W.; Liao, Y.; Li, P.; Garibay, S. J.; Zhang, X.; DeStefano, M. R.; Hupp, J. T.; et al. Room Temperature Synthesis of an 8-Connected Zr-Based Metal-Organic Framework for Top-Down Nanoparticle Encapsulation. *Chem. Mater.* **2018**, *30*, 2193–2197.
- (29) Goswami, S.; Ray, D.; Otake, K.-i.; Kung, C.-W.; Garibay, S. J.; Islamoglu, T.; Atilgan, A.; Cui, Y.; Cramer, C. J.; Farha, O. K.; et al. A Porous, Electrically Conductive Hexa-Zirconium(IV) Metal-Organic Framework. *Chem. Sci.* **2018**, *9*, 4477–4482.
- (30) Osterieth, J. W. M.; Wright, D.; Noh, H.; Kung, C.-W.; Vulpe, D.; Li, A.; Park, J. E.; Van Duyne, R. P.; Moghadam, P. Z.; Baumberg, J. J.; et al. Core-Shell Gold Nanorod@Zirconium-Based Metal-Organic Framework Composites as In Situ Size-Selective Raman Probes. *J. Am. Chem. Soc.* **2019**, *141*, 3893–3900.
- (31) Inukai, M.; Fukushima, T.; Hijikata, Y.; Ogiwara, N.; Horike, S.; Kitagawa, S. Control of Molecular Rotor Rotational Frequencies in Porous Coordination Polymers Using a Solid-Solution Approach. *J. Am. Chem. Soc.* **2015**, *137*, 12183–12186.

- (32) Kozachuk, O.; Meilikhov, M.; Yussenko, K.; Schneemann, A.; Jee, B.; Kuttathayil, A. V.; Bertmer, M.; Sternemann, C.; Pöppel, A.; Fischer, R. A. A Solid-Solution Approach to Mixed-Metal Metal-Organic Frameworks - Detailed Characterization of Local Structures, Defects and Breathing Behaviour of Al/V Frameworks. *Eur. J. Inorg. Chem.* **2013**, 2013, 4546–4557.
- (33) Mohammad-Pour, G. S.; Hatfield, K. O.; Fairchild, D. C.; Hernandez-Burgos, K.; Rodríguez-López, J.; Uribe-Romo, F. J. A Solid-Solution Approach for Redox Active Metal-Organic Frameworks with Tunable Redox Conductivity. *J. Am. Chem. Soc.* **2019**, 141, 19978–19982.
- (34) Fei, H.; Han, C. S.; Robins, J. C.; Oliver, S. R. J. A Cationic Metal-Organic Solid Solution Based on Co(II) and Zn(II) for Chromate Trapping. *Chem. Mater.* **2013**, 25, 647–652.
- (35) Chen, T.; Dou, J.-H.; Yang, L.; Sun, C.; Libretto, N. J.; Skorupskii, G.; Miller, J. T.; Dincă, M. Continuous Electrical Conductivity Variation in $M_3(\text{Hexaiminotriphenylene})_2$ ($M = \text{Co}, \text{Ni}, \text{Cu}$) Mof Alloys. *J. Am. Chem. Soc.* **2020**, 142, 12367–12373.
- (36) Kung, C.-W.; Wang, T. C.; Mondloch, J. E.; Fairen-Jimenez, D.; Gardner, D. M.; Bury, W.; Klingsporn, J. M.; Barnes, J. C.; Van Duyn, R.; Stoddart, J. F.; et al. Metal-Organic Framework Thin Films Composed of Free-Standing Acicular Nanorods Exhibiting Reversible Electrochromism. *Chem. Mater.* **2013**, 25, 5012–5017.
- (37) Mondloch, J. E.; Bury, W.; Fairen-Jimenez, D.; Kwon, S.; DeMarco, E. J.; Weston, M. H.; Sarjeant, A. A.; Nguyen, S. T.; Stair, P. C.; Snurr, R. Q.; et al. Vapor-Phase Metalation by Atomic Layer Deposition in a Metal-Organic Framework. *J. Am. Chem. Soc.* **2013**, 135, 10294–10297.
- (38) Ma, J.; Tran, L. D.; Matzger, A. J. Toward Topology Prediction in Zr-Based Microporous Coordination Polymers: The Role of Linker Geometry and Flexibility. *Cryst. Growth Des.* **2016**, 16, 4148–4153.
- (39) Pang, J.; Yuan, S.; Qin, J.; Liu, C.; Lollar, C.; Wu, M.; Yuan, D.; Zhou, H.-C.; Hong, M. Control the Structure of Zr-Tetracarboxylate Frameworks through Steric Tuning. *J. Am. Chem. Soc.* **2017**, 139, 16939–16945.
- (40) Holder, C. F.; Schaak, R. E. Tutorial on Powder X-Ray Diffraction for Characterizing Nanoscale Materials. *ACS Nano* **2019**, 13, 7359–7365.
- (41) Yeung, H. H. M.; Li, W.; Saines, P. J.; Köster, T. K. J.; Grey, C. P.; Cheetham, A. K. Ligand-Directed Control over Crystal Structures of Inorganic-Organic Frameworks and Formation of Solid Solutions. *Angew. Chem., Int. Ed.* **2013**, 52, 5544–5547.
- (42) Akkerman, Q. A.; D'Innocenzo, V.; Accornero, S.; Scarpellini, A.; Petrozza, A.; Prato, M.; Manna, L. Tuning the Optical Properties of Cesium Lead Halide Perovskite Nanocrystals by Anion Exchange Reactions. *J. Am. Chem. Soc.* **2015**, 137, 10276–10281.
- (43) Sun, D.; Sun, F.; Deng, X.; Li, Z. Mixed-Metal Strategy on Metal-Organic Frameworks (MOFs) for Functionalities Expansion: Co Substitution Induces Aerobic Oxidation of Cyclohexene over Inactive Ni-Mof-74. *Inorg. Chem.* **2015**, 54, 8639–8643.
- (44) Lee, G.; Lee, S.; Oh, S.; Kim, D.; Oh, M. Tip-to-Middle Anisotropic MOF on-MOF Growth with a Structural Adjustment. *J. Am. Chem. Soc.* **2020**, 142, 3042–3049.
- (45) Albo, J.; Perfecto-Irigaray, M.; Beobide, G.; Irabien, A. Cu/Bi Metal-Organic Framework-Based Systems for an Enhanced Electrochemical Transformation of CO_2 to Alcohols. *J. of CO_2 Util.* **2019**, 33, 157–165.
- (46) Liu, C.; Sun, Q.; Lin, L.; Wang, J.; Zhang, C.; Xia, C.; Bao, T.; Wan, J.; Huang, R.; Zou, J.; et al. Ternary MOF-on-MOF Heterostructures with Controllable Architectural and Compositional Complexity Via Multiple Selective Assembly. *Nat. Commun.* **2020**, 11, 4971.
- (47) Choi, S.; Kim, T.; Ji, H.; Lee, H. J.; Oh, M. Isotropic and Anisotropic Growth of Metal-Organic Framework (Mof) on Mof: Logical Inference on MOF Structure Based on Growth Behavior and Morphological Feature. *J. Am. Chem. Soc.* **2016**, 138, 14434–14440.
- (48) Yuan, S.; Qin, J.-S.; Li, J.; Huang, L.; Feng, L.; Fang, Y.; Lollar, C.; Pang, J.; Zhang, L.; Sun, D.; et al. Retrosynthesis of Multi-Component Metal-Organic Frameworks. *Nat. Commun.* **2018**, 9, 808.
- (49) Zhang, D.; Zhu, Y.; Liu, L.; Ying, X.; Hsiung, C.-E.; Sougrat, R.; Li, K.; Han, Y. Atomic-Resolution Transmission Electron Microscopy of Electron Beam-Sensitive Crystalline Materials. *Science* **2018**, 359, 675.
- (50) He, T.; Ni, B.; Zhang, S.; Gong, Y.; Wang, H.; Gu, L.; Zhuang, J.; Hu, W.; Wang, X. Ultrathin 2D Zirconium Metal-Organic Framework Nanosheets: Preparation and Application in Photocatalysis. *Small* **2018**, 14, 1703929.
- (51) Xu, M.; Meng, S.-S.; Cai, P.; Tang, W.-Q.; Yin, Y.-D.; Powell, J. A.; Zhou, H.-C.; Gu, Z.-Y. Modulating the Stacking Modes of Nanosized Metal-Organic Frameworks by Morphology Engineering for Isomer Separation. *Chem. Sci.* **2021**, 12, 4104–4110.
- (52) Tang, W.-Q.; Zhao, Y.-J.; Xu, M.; Xu, J.-Y.; Meng, S.-S.; Yin, Y.-D.; Zhang, Q.-H.; Gu, L.; Liu, D.-H.; Gu, Z.-Y. Controlling the Stacking Modes of Metal-Organic Framework Nanosheets through Host-Guest Noncovalent Interactions. *Angew. Chem., Int. Ed.* **2021**, 60, 6920–6925.